ADVANCED ENERGY MATERIALS
www.advenergymat.de

Microstructure of Lithium Metal Electrodeposited at the Steel|Li_6PS_5Cl Interface in "Anode-Free" Solid-State Batteries

Juri Becker, Till Fuchs, Till Ortmann, Sascha Kremer, Felix H. Richter, and Jürgen Janek**

Recent research shows that integrating lithium metal anodes can enhance battery energy density, but the high reactivity of lithium requires handling under inert conditions to avoid degradation. To overcome this, reservoir-free cells (RFCs) are explored, where lithium metal is electrodeposited at the current collector (CC) and solid electrolyte (SE) interface during initial charging. The electrochemical properties of electrodeposited lithium are influenced by its morphology and microstructure, which impact lithium discharge capacity and pore formation. However, little is known about how to control the microstructure of electrodeposited lithium. This work experimentally characterizes the lithium microstructure at the steel|Li_6PS_5Cl interface using cryogenic ion beam milling, scanning electron microscopy (SEM), and electron backscatter diffraction (EBSD), focusing on the effects of electrodeposition current density and lithium layer thickness. The results show that layer thickness, not current density, primarily governs the lithium microstructure. This "specimen thickness effect" is qualitatively described using a Monte Carlo Potts model and indicates that electrodeposited lithium metal quickly equilibrates at room temperature.

1. Introduction

Solid-state batteries (SSBs) are of primary interest as alternatives to conventional lithium-ion batteries as solid electrolytes (SEs) may enable the use of lithium metal as negative electrode material.[1,2] Having a low redox potential of −3.04 V and a high theoretical specific capacity of 3861 mAh g^{-1}, the implementation of lithium metal would significantly increase the energy storage capability of next-generation rechargeable batteries, while SEs are expected to meet future safety standards.[3–5]

As lithium is highly reactive, degradation layers form on the surface of pristine foils when in contact with atmospheric constituents or SEs.[6–9] To minimize the thickness of this degradation layer, storage under the exclusion of nitrogen, oxygen, and water is necessary. However, even in argon-filled gloveboxes with low partial pressures of reactive gases, degradation layers still form.[6] These layers increase the resistance of lithium|SE interfaces, and significantly impact the electrochemical performance. To reduce this interfacial resistance, either high pressures of ≈400 MPa must be applied during preparation, or mechanical cleaning steps must be used to remove the degradation layers from the lithium surface beforehand. Both methods, as well as storage under inert gas, are costly and impede manufacturing.[8,10]

To circumvent the challenging reactivity of lithium metal foils, avoid costly storage under an inert atmosphere, and further increase the theoretical energy density, reservoir-free cells (RFCs, often referred to as "anode-free") are increasingly investigated and developed.[7,11–13] Directly after cell assembly, RFCs consist in their discharged state only of lithiated positive electrode material, SE, and current collectors (CC). Their distinctive feature is that the CC at the negative electrode is in direct contact with the SE separator layer. No reservoir of lithium at the negative electrode is added, as the lithium available for cycling is contained in the lithiated active material in the positive electrode.[14,15] Lithium metal is electrodeposited on the CC during the first charging step, with 5 µm of electrodeposited lithium corresponding to roughly 1 mAh cm^{-2} of capacity. As a result, the reservoir-free electrode further increases the energy density compared to SSBs with an additional lithium layer.[11] Sufficiently stable cells require a very high Coulomb efficiency,[16] and ≈20 µm of lithium need to be reversibly cycled to meet an areal capacity of 4 mAh cm^{-2}.

The microstructure of electrodeposited lithium is of great interest because it influences the Coulomb efficiency, as shown by Singh et al. in Li|LLZO|Li cells.[17,18] Under pressure, large-grained lithium foils exhibit higher stripping capacities and an increased electrode roughness after contact loss, while smaller-grained lithium foils have lower stripping capacities and a smoother electrode surface after contact loss. Moreover, it has been established that the lithium microstructure significantly impacts both its mechanical and electrochemical properties during

J. Becker, T. Fuchs, T. Ortmann, S. Kremer, F. H. Richter, J. Janek
Institute of Physical Chemistry and Center for Materials Research (ZfM)
Justus-Liebig-University Giessen
Heinrich-Buff-Ring 17, D-35392 Giessen, Germany
E-mail: till.fuchs@phys.chemie.uni-giessen.de;
juergen.janek@phys.chemie.uni-giessen.de

The ORCID identification number(s) for the author(s) of this article can be found under https://doi.org/10.1002/aenm.202404975

DOI: 10.1002/aenm.202404975

cycling as an anode material, when using foils.[19–21] However, the microstructure of lithium foils is not tangible, as it is largely dependent on industrial manufacturing processes.

No lithium metal is required for the construction of RFCs, which simplifies the supply chain and storage beforehand. Additionally, electrodeposition allows for homogeneous lithium|SE interface contacts even at low stack pressures, in the range of 10 MPa or less, and enables precise determination of the battery's start of service life.[11,22] We like to note that conventional lithium-ion batteries (LIBs) operate similarly with respect to the lithium inventory, as also here all lithium is initially stored in the positive electrode and transferred to the negative (graphite) electrode during the first charge step. Thus, balancing the lithium inventory in "reservoir-free" SSBs and minimizing the loss of lithium in any SEI is as relevant as in LIBs.[23–25]

The primary challenge with RFCs arises from the morphology of the electrodeposited lithium layer, often resulting in non-uniform lithium structures in the form of islands, dendrites, or whiskers.[26–30] Recent research indicates that external factors such as temperature, stack pressure, and current density can significantly impact the morphology of the electrodeposited lithium layer.[22,31–34] For example, a higher electrodeposition current density leads to an increased nucleation density, leading to higher coverage of the current collector.[22,31,32] The resulting microstructure of lithium layers electrodeposited in RFCs is a largely unexplored parameter although it has a large influence on the electrochemical and chemo-mechanical properties of the alkali metal.[18,19,35]

As shown in previous reports, the microstructure of metals, including lithium, can be analyzed using electron backscatter diffraction (EBSD) without the influence of the analysis method itself.[19,36–39] Going beyond the characterization of conventional metal foils, Fuchs and Ortmann et al. reported a well-reproducible workflow and presented a qualitative microstructure analysis of electrodeposited lithium by EBSD.[39] They showed that the microstructure of electrodeposited lithium does not change over time at room temperature,[39] allowing to analysis of electrodeposited lithium as a function of different electrodeposition parameters.

To the best of our knowledge, the influence of electrodeposition parameters on the lithium microstructure has not been studied yet, due to the buried nature of interfaces and the high reactivity of the metal during sample preparation. The electrodeposition of other metals such as Cu, Ag, or alloys like $Ni_{0.2}Co_{0.8}$ at liquid|solid interfaces, shows a correlation between the used electrodeposition parameters and the resulting microstructure, which in turn suggests that also the microstructure of electrodeposited lithium depends on the electrodeposition parameters.[37,40,41]

Electrodeposition of lithium with controlled microstructure could be an effective method of modifying the cycling properties of the lithium electrode. By varying electrodeposition parameters such as current density, temperature, or capacity, microstructural parameters such as grain size or grain boundary distribution might be adjusted, potentially adapting the microstructure to the requirements for further cell operation.

This work aims to better understand the microstructure of lithium layers electrodeposited at the interface between steel and Li_6PS_5Cl as a function of the current density used for electrodeposition and to analyze the microstructural evolution during prolonged lithium electrodeposition, i.e., for different lithium layer thicknesses. The preparation of wide cross-sections allows for the analysis of many grains and obtain reliable statistics regarding grain size and grain orientation. In the second step, the experimental results are described with a Monte Carlo Potts model. The results reveal that the microstructure of electrodeposited lithium layers is mostly independent of the current density, i.e., electrodeposition kinetics. There is rather a specimen thickness effect, i.e., the layer thickness determines the lithium microstructure, offering to effectively adjust the microstructure of electrodeposited lithium to match requirements for further cell operation (i.e., lithium dissolution) by changing electrodeposition capacities.

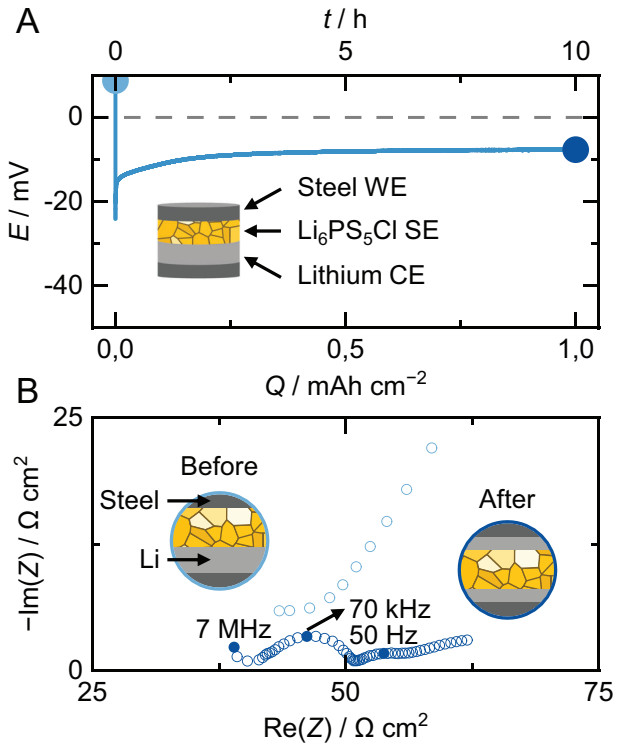

Figure 1. Illustration of the model system used and a representative lithium electrodeposition. A) Voltage profile of lithium electrodeposition at the steel|Li_6PS_5Cl interface using a current density of 100 µA cm^{-2} and schematic of the used cell setup steel|Li_6PS_5Cl|Li|steel. B) Impedance data before and after the electrodeposition of lithium at the steel|Li_6PS_5Cl interface, as depicted in the schemes. Characteristic frequencies are highlighted with filled circles. The time of the measurement is marked in the voltage profile with enlarged dots.

2. Results and Discussion

2.1. Electrodeposition of Lithium at the Steel|Li_6PS_5Cl Interface

To investigate the influence of electrodeposition parameters on the lithium microstructure, we built steel|Li_6PS_5Cl|Li|steel cells to be used as a model system. A characteristic voltage profile for lithium electrodeposition at the steel|Li_6PS_5Cl interface with a current density of 100 µA cm^{-2} is shown in **Figure 1A**. First, the voltage profile passes through a minimum, which represents

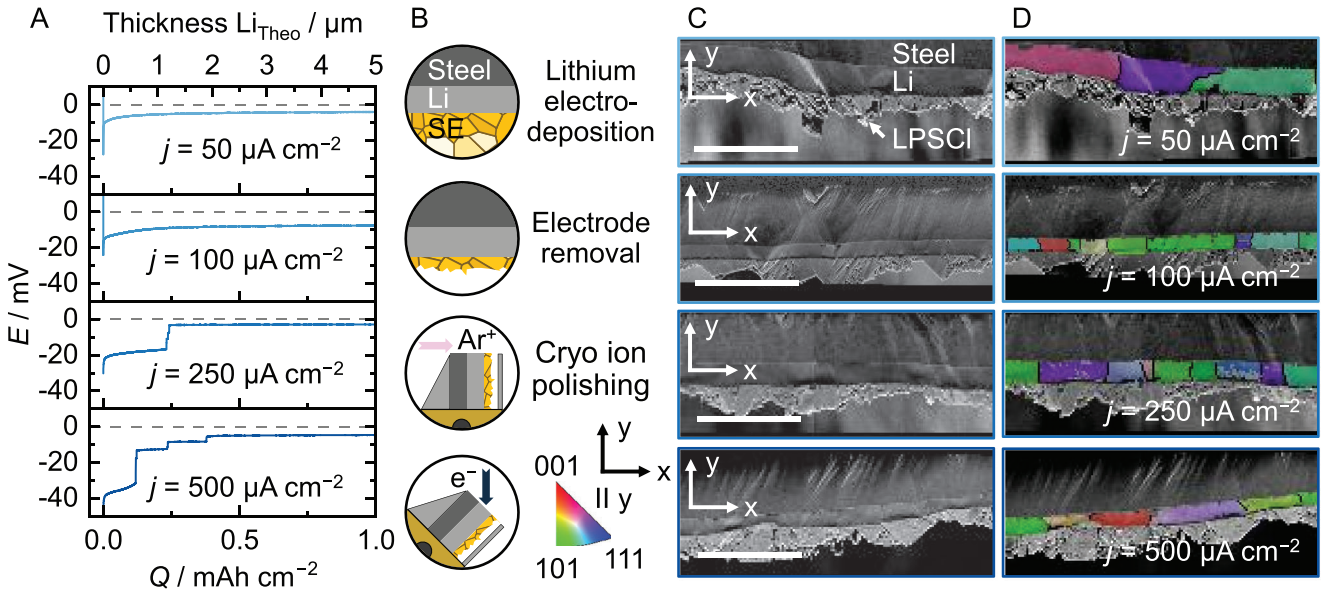

Figure 2. Current density-dependent lithium electrodeposition and microstructural analysis. A) Voltage profiles during lithium electrodeposition with current densities between 50 µA cm^{-2} and 500 µA cm^{-2} as well as the calculated lithium layer thickness. B) Schematic of the used workflow to prepare cross-sections. C) SEM images of representative steel|Li_6PS_5Cl cross-sections after electrodeposition of lithium with different current densities, see also Figures S1–S4 (Supporting Information). D) Overlay of the SEM images and IPF maps, which are given parallel to the y-direction as illustrated in (B). Grain boundaries (> 10°) are depicted with black lines. Misorientations between 2° and 10° are depicted in grey. The scale bar within the SEM images represents a length of 50 µm and also applies to the respective image overlayed with its IPF map.

the nucleation overvoltage relative to the following plateau, being in good agreement with previous studies on the electrodeposition of lithium at CC|SE interfaces.[11,31] Here, lithium nucleation occurs.[11] The voltage then stabilizes at ≈10 mV, which agrees with the IR drop of the solid electrolyte. At this point, the previously formed nuclei grow larger, forming the observed grains.[11] Deviations stem from the resistances occurring at the two Li|Li_6PS_5Cl interfaces.

Additionally, exemplary impedance plots in Nyquist representation before and after the electrodeposition are shown in Figure 1B, recorded at the times indicated with two enlarged points within the voltage curve. The steel electrode is initially an ion-blocking electrode, which is why a capacitive response before electrodeposition is visible at lower frequencies (<3 MHz). After electrodeposition, the cell has two lithium electrodes (i.e., two reversible electrodes for lithium ions), as indicated in the schematics in (B). As a result, several semicircles are now observed within the impedance data, which can be attributed to the charge transfer at the two Li|Li_6PS_5Cl interfaces, proving successful lithium electrodeposition.[11]

The resistance contribution of the solid electrolyte has not changed significantly during nucleation and growth, indicating that no severe lithium electrodeposition or dendrite formation has taken place inside the solid electrolyte. However, due to a similar resistance contribution of thin lithium filaments and Li_6PS_5Cl, partial dendrite formation or lithium deposition inside of the Li_6PS_5Cl pellet cannot be completely ruled out. Nevertheless, the used model system is suited for investigating the electrodeposition of lithium with different current densities, which is presented in the following section.

2.2. Influence of Current Density on the Lithium Microstructure

Voltage profiles for lithium electrodeposition with 50 µA cm^{-2}, 100 µA cm^{-2}, 250 µA cm^{-2}, and 500 µA cm^{-2}, as well as exemplary SEM pictures and inverse pole figure (IPF) maps of the prepared cross-sections of the different layers are shown in **Figure 2**. Electrodeposition was limited to a capacity of 1 mAh cm^{-2}, theoretically resulting in a lithium layer thickness d_{Layer} of 5 µm. Please note that the charge per area is referred to as capacity in accordance with literature.

As in Figure 1A, the voltage profiles show a characteristic minimum, which represents the nucleation overvoltage when referenced to the following plateau. Electrodepositing lithium with current densities of 50 µA cm^{-2} and 100 µA cm^{-2} results in a continuous voltage profile during the electrodeposition process after nucleation. However, for higher current densities of 250 µA cm^{-2} and 500 µA cm^{-2}, discontinuities occur in the voltage profile. These are caused by dendrite formation, as lithium filaments from the metal anode penetrate the solid electrolyte and (soft)-short-circuit the cell. This phenomenon is known for lithium metal anodes–especially at higher current densities–and resembles one of the main challenges for the initial charging step in RFCs if high areal capacities are applied.[42,43]

Nevertheless, a dense and homogeneous lithium layer is observed for all current densities in the SEM images. The prepared cross-sections show a layered electrode arrangement, with the steel foil at the top, which was used as the WE as shown in Figure 1A. The electrodeposited lithium layer can be seen below. At the bottom, residual SE remains adhered to the electrode during cell disassembly. It is noteworthy that in all cases a homogeneous lithium layer had grown over almost the entire

width of the prepared cross-section (over several millimeters). For the full cross-section, we refer to the Supporting Information (Figures S1–S4, Supporting Information). Furthermore, homogeneous Li|Li_6PS_5Cl and Li|steel interfaces are visible along the entire cross-section, revealing continuous physical contact between the materials.

To exclude the influence of the layer thickness as much as possible, layers of approximately the same thickness d_{Layer} were electrodeposited. The thicknesses of the electrodeposited lithium should theoretically be roughly 5 µm for $Q = 1$ mAh cm^{-2}. When compared with the SEM images, lithium layers thicker than 5 µm are found for all used current densities, as lithium is only electrodeposited on part of the electrode area, as can be seen in optical images of the SE pellet surface and working electrode surface of a similar sample in Figure S5 (Supporting Information). Interestingly, even for the cells in which a short circuit occurred during electrodeposition (i.e. $j = 250$ µA cm^{-2} and 500 µA cm^{-2}), a layer thickness larger than 5 µm is visible. In addition to the deviation between the total and used electrode area, another reason could be that even after the first discontinuity in the voltage profile, further lithium electrodeposition occurs, as only a "soft short" has been created. In this case, the resistance of the existing dendrite is approximately as high as the resistance of the solid electrolyte, so that current continues to be transported in the form of lithium ions.[3] This is proven by further discontinuities, which are caused by further redox reactions at the electrodes (i.e., ongoing dendrite formation).

Analysis of the electrodeposited lithium layer via EBSD enables direct visualization of the different grains formed during electrodeposition. Different grains are colored according to an inverse pole figure color scheme in the *y*-direction (growth direction), i.e., each pixel is colored according to the crystal direction that runs parallel to the *y*-direction of the map. Noticeably, most grain boundaries are oriented perpendicular to the steel|Li_6PS_5Cl interface. This is particularly interesting as it represents a major difference to conventionally prepared Li_{foil}|Li_6PS_5Cl interfaces. The grains of conventional lithium foils are usually oriented randomly,[39] resulting in the presence of both vertical and parallel grain boundaries within the lithium metal attached to the SE. This has probably a significant influence on the dissolution of lithium after electrodeposition and the mechanics of the electrode.

For comparison of the different current densities and to include statistics, the dimensions for all analyzed grains are summarized within a boxplot in **Figure 3**. At this point, it should be noted that when analyzing the grains, grains located at the edge of the cross-section were not considered if they were not visible over their entire width. Using millimeter-sized cross-sections, 70 grains were analyzed for a current density of 50 µA cm^{-2}, 59 for 100 µA cm^{-2}, 109 for 250 µA cm^{-2} and 51 for 500 µA cm^{-2}. The boxplot in blue summarizes the measured grain widths w_{Grain} for the different current densities. It should be noted that the grain width w_{Grain} refers to the lateral dimension of the grains along the cross-section. Due to the slight deviation in layer thicknesses, as can be seen in Figure 3 in black above, we herein excluded the vertical dimension of the analyzed grains. Furthermore, we assumed for simplicity that the grains´ cross-sections are rectangles, which only leads to negligibly small deviations in width due to the mostly vertical grain boundaries. Taking the cross-sectional

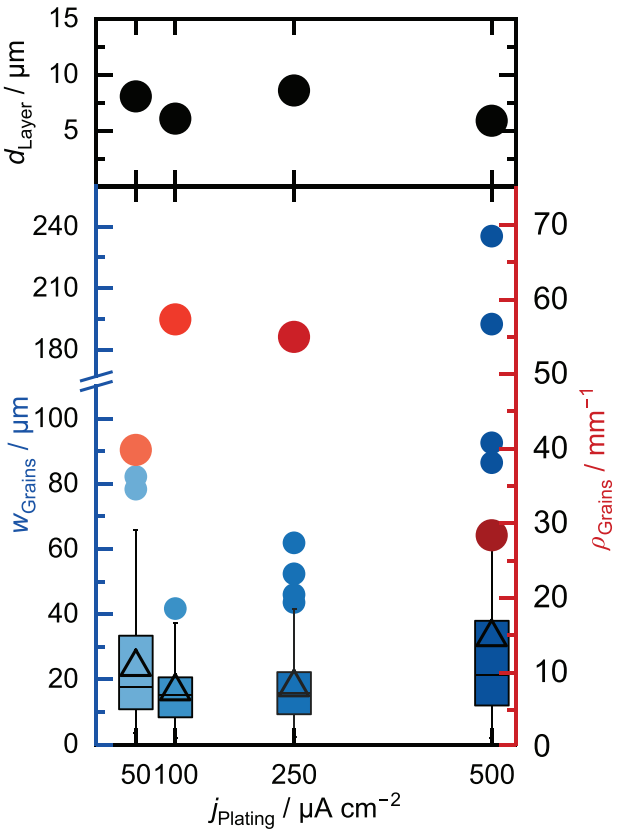

Figure 3. Summary of the analyzed lithium layers electrodeposited with different current densities. The average layer thickness is shown in black circles in the top part of the graph. The width of each lithium grain (w_{Grains}) as well as the calculated grain density (ρ_{Grains}) are depicted in the section beneath. The distribution of grain widths is shown in the boxplot in blue and summarizes 70 (50 µA cm^{-2}), 59 (100 µA cm^{-2}), 109 (250 µA cm^{-2}), and 51 (500 µA cm^{-2}) measured grains, respectively. The average width is represented with a triangle inside each box. Outliers (interquartile range factor = 1.5) are marked with blue points. The calculated grain density is depicted in red.

length into account, the grain density, i.e., the number of grains per millimeter of cross-section, was also calculated. This is shown in red.

From previous works on RFCs, it is known that an increased current density increases the nucleation density.[22,31] If the microstructure of a lithium layer were determined by nucleation solely, one would expect that a higher current density would also lead to a smaller grain size and a higher grain density ρ_{Grains}. At this point, we like to note that the published nucleation experiments were carried out with Cu|$Li_{6.25}Al_{0.25}La_3Zr_2O_{12}$ and Cu|LiPON model systems. As a first approximation, however, we assume that the steel|Li_6PS_5Cl system used here follows a similar current density dependence – even though copper and steel interact differently with lithium metal, as copper, unlike steel, can dissolve lithium.[44] Due to the method of analysis (i.e., in a cross-sectional way), the data are referenced to a width instead of an area here.

When comparing the expected nucleation density and the resulting number of grains for the different current densities, however, a significant difference between the two quantities

shows up. Compared to an expected number of nuclei[22] of around 320 mm^{-1} for 50 µA cm^{-2} and 700 nuclei per mm for 500 µA cm^{-2}, we measured a considerably smaller grain density ρ_{Grains} of 40 grains per mm for 50 µA cm^{-2} and 28 grains per mm for 500 µA cm^{-2}. Notably, these values cannot be directly compared, as not every nucleus results in a separate grain; neighboring nuclei may merge due to similar orientations to form a single grain upon contact. However, the difference of an order of magnitude strongly hints toward an influence of the subsequent grain growth after nucleation.

When comparing different current densities, no significant trend is found. The average grain width, marked with triangles, remains ≈20 µm for all current densities, with deviations falling within the range of measurement accuracy or within statistical variation. The grain density ρ_{Grains}, displayed in red, behaves analogously and shows no clear trend for the used current densities. Interestingly, both w_{Grain} and ρ_{Grains} are highest and lowest for 500 µA cm^{-2} respectively. The exact opposite would have been expected under the assumption that the nucleation density is highest for 500 µA cm^{-2}.

In summary, the microstructure of electrodeposited lithium layers seems not to be solely determined by nucleation. Otherwise, a stronger correlation between the electrodeposition current density and the resulting grain size or grain density would arise. However, it should be noted that due to experimental limitations, the layers were only analyzed after the deposition of 1 mAh cm^{-2}. Thus, grain growth might have already taken place during deposition. The steel foil substrate appears to have no significant influence on the lithium microstructure. Compared to the average grain size of the steel foil, those determined for lithium are much larger (see Figure S6, Supporting Information). This is in good agreement with previous results of electrodeposited alkaline metal layers on different substrates.[39] An influence of the Li_6PS_5Cl SE on the nucleation or the microstructure shortly after the start of electrodeposition cannot be ruled out and is further discussed based on our simulations in the respective chapter. Possible further effects on the microstructure include the stack pressure that was applied to the cell during electrodeposition. More likely, however, is relatively fast lateral grain growth during continuous lithium electrodeposition, i.e., during vertical layer growth, which is examined in more detail below.

2.3. Influence of Electrodeposition Capacity on the Lithium Microstructure

First investigations by Fuchs and Ortmann et al. on electrodeposited alkali metal layers in an *operando* experiment already suggest that the microstructure is not solely determined by the initial nucleation of lithium. Instead, lateral grain growth appears to occur during ongoing electrodeposition.[39] This agrees with the results summarized in the previous section. Hence, the microstructural evolution of lithium layers during prolonged electrodeposition is examined in the following.

For this, the capacity Q was increased to 2.5 mAh cm^{-2}, 5 mAh cm^{-2}, and 10 mAh cm^{-2} in additional measurements, changing the theoretical (mean) layer thickness from 5 up to 50 µm, respectively, while keeping the current density constant at 100 µA cm^{-2}. The voltage profiles during electrodeposition and examples of the subsequent SEM analysis combined with EBSD are shown in **Figure 4**.

As with the first electrodeposition, a continuous profile can be seen in Figure 4A. For none of the selected capacities a short circuit occurs, showing that even thick lithium layers can be electrodeposited free of short-circuits with 100 µA cm^{-2} at the steel|Li_6PS_5Cl interface. The measured layer thickness compared to the theoretically expected one is shown in Figure 4B. As discussed before, the actual thickness is slightly higher compared to the calculated one, due to the incomplete coverage of the steel electrode size. Interestingly, the largest deviation between the measured and theoretical values occurs at Q = 10 mAh cm^{-2}. This may be due to an uneven growth rate of certain areas of the layer, caused by an inhomogeneous stack pressure distribution during electrodeposition. The uneven stack pressure distribution could either stem from cell preparation or faster growth in some areas, leading to poorer contact between the steel stamp and working electrode in slower-growing regions. Deviations in thickness align with observations of another thick lithium layer, where thinning occurs at the edges of the electrode (see Figure S7, Supporting Information).

Analysis of the electrodeposited lithium within the SEM reveals a dense layer in the region of interest, with only small local differences in layer thickness. For a complete view of the cross-section, the reader is referred to Figures S2, S8–S10 (Supporting Information). All layers retain the columnar structure, with almost exclusively vertical grain boundaries and grains spanning the entire layer thickness. Occasionally, as seen in the center of the IPF map for Q = 10 mAh cm^{-2} (see Figure 4D), smaller truncated grains appear between two larger neighboring grains. These V-shaped grains might result from the preferential growth of certain grains during prolonged electrodeposition or due to significant differences in growth rates. Their number is typically small.[39]

When comparing the individual layers, both the grain height h_{Grains} and the grain width w_{Grains} differ between layers. For lower capacities, multiple grains are fully visible in the chosen image section in Figure 4D. The higher the capacity, the fewer grains are visible. For a more in-depth analysis, all grains are characterized both in terms of their grain height h_{Grains}, and their width w_{Grains}. For a capacity of 1 mAh cm^{-2}, the number of grains amounts to 59, for 2.5 mAh cm^{-2} to 54, for 5 mAh cm^{-2} to 21, and for 10 mAh cm^{-2} to 16.

To gain a better understanding of possible deformations or stresses within the electrodeposited lithium grains, they were further analyzed for their misorientation. The measure used for this is the grain reference orientation deviation (GROD) angle, which indicates the misorientation of a pixel within the grain relative to the average orientation of the entire grain.[45–49] The resulting boxplots, the calculated grain density ρ_{Grains} per mm cross-section, and the measured GROD angles are shown in **Figure 5**. As before, please note that partially visible grains located at the edge of the cross-section were not considered.

The upper boxplot, which shows the grain height, reveals that almost all grains in the individual layers have a similar height. The fact that the height of all grains approximately corresponds to the layer thickness (see Figure 4B), shows that the columnar structure is preserved for all electrodeposited layer thicknesses and that almost all grains span the entire layer thickness. For

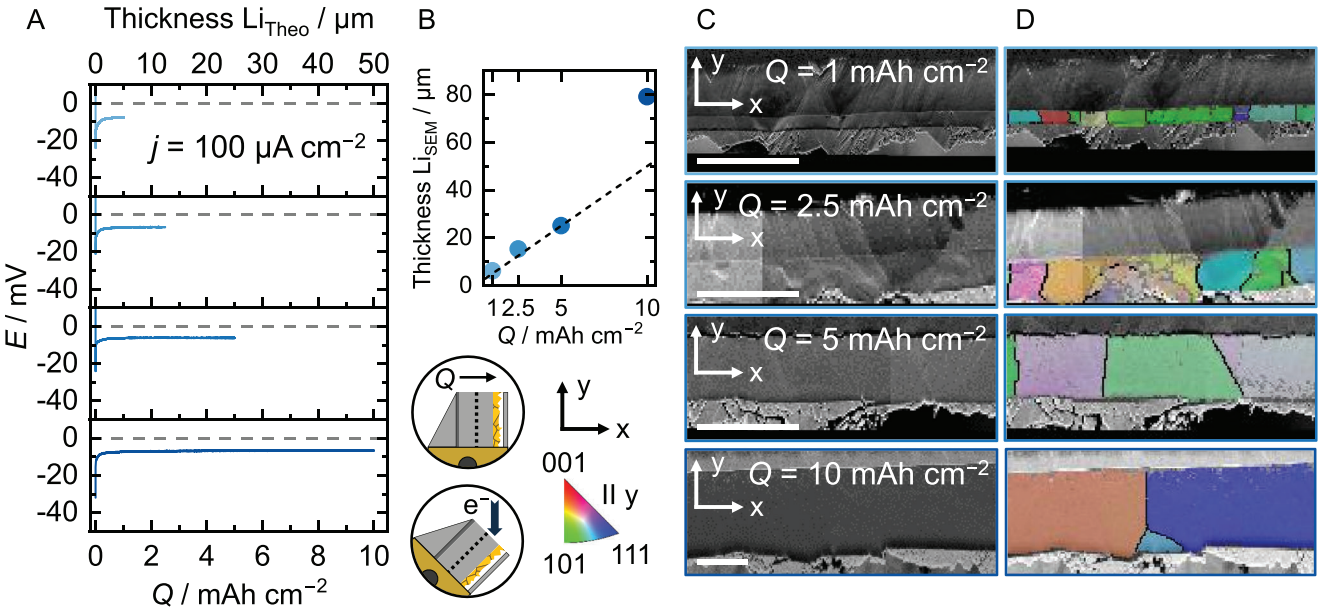

Figure 4. Layer thickness-dependent lithium electrodeposition and microstructural analysis. A) Voltage profiles during electrodeposition for four different capacities (1 mAh cm^{-2}, 2.5 mAh cm^{-2}, 5 mAh cm^{-2}, and 10 mAh cm^{-2}) using a current density of 100 µA cm^{-2}. Please note that the sample for Q = 1 mAh cm^{-2} is the same one as in Figure 2, inserted here for direct comparison. B) Layer thickness determined by SEM, in which the expected theoretical thickness is depicted as a dotted line. A sketch of the following EBSD analysis is shown below. C) SEM images of representative steel|Li_6PS_5Cl cross-sections after electrodeposition of lithium for different capacities, see also Figures S2, S8–S10 (Supporting Information). D) Overlay of the SEM images and IPF maps, which are given parallel to the y-direction as illustrated in (B). Grain boundaries (> 10°) are depicted with black lines. Misorientations between 2° and 10° are depicted in grey. The scale bar within the SEM images represents a length of 50 µm and also applies to the respective image overlayed with its IPF map.

Q = 10 mAh cm^{-2}, two outliers are found, which can be attributed to the truncated grains mentioned above.

There is a strong increase in the grain width with increasing layer thickness. While the average grain width for Q = 1 mAh cm^{-2} is 16 µm, this increases to 194 µm for Q = 10 mAh cm^{-2}. The same applies to the grain density, for a capacity of Q = 1 mAh cm^{-2} this is calculated to be 57 grains per mm. At Q = 10 mAh cm^{-2}, the density decreases to 5 grains per mm, revealing a strong correlation between layer thickness and the resulting microstructure. This effect seems to be evident within individual lithium layers as well: the grain size appears to decrease in thin regions of an otherwise thick lithium layer (see Figure S7, Supporting Information). Additionally, the microstructure of the steel foil does not affect the microstructure of lithium at the investigated layer thicknesses, since the microstructure of lithium changes significantly while the steel foil is assumed to remain unchanged.

To investigate the influence of electrodeposition time and resulting microstructure, another lithium layer with a capacity of 1 mAh cm^{-2} was electrodeposited at a current density of 10 µA cm^{-2}, requiring 100 h (see Figure S11, Supporting Information). This matches the electrodeposition time for the layer with a capacity of Q = 10 mAh cm^{-2} electrodeposited with 100 µA cm^{-2}. As shown in Figures S12, S13 (Supporting Information), the resulting microstructure of the layer electrodeposited with 10 µA cm^{-2} for a capacity of Q = 1 mAh cm^{-2} is almost identical to the other lithium layers with a capacity of Q = 1 mAh cm^{-2}.

This indicates that rather the electrodeposited capacity, and not the electrodeposition time, influences the microstructure. Additionally, our hypothesis from the previous section that the current density does not significantly affect the microstructure is confirmed. However, it is important to note that all lithium layers were analyzed after a certain deposition, storage, and preparation time. This means that no reliable statement can be made about the initial structure of the lithium layers. Results of *operando* experiments by Fuchs and Ortmann et al. indicate that the grains grow rapidly during electrodeposition, which means that in all cases we are likely analyzing a lithium layer in its fully annealed, i.e., equilibrium state.

Furthermore, this explains why no significant change in the microstructure could be observed in the current density-dependent experiments, even though different nucleation densities are expected. The grain growth following nucleation leads to certain grains preferentially growing both vertically and laterally. During this grain growth, certain grains are consumed, causing the mean lateral grain size to increase and grain density to decrease. This growth could be caused by a mechanism similar to grain ripening or "secondary recrystallization", as suggested by Fuchs and Ortmann et al. The driving force is the natural tendency to minimize interfacial and grain boundary energies.[50,51] Here, it should be noted that room temperature (25 °C) corresponds to a homologous temperature of T_H = 0.66 for lithium, indicating that room temperature operation of lithium corresponds in principle to a *high-temperature* process, likely increasing the grain boundary velocity. Recrystallization in metals typically occurs at homologous temperatures between 0.4 and 0.6.[52] This

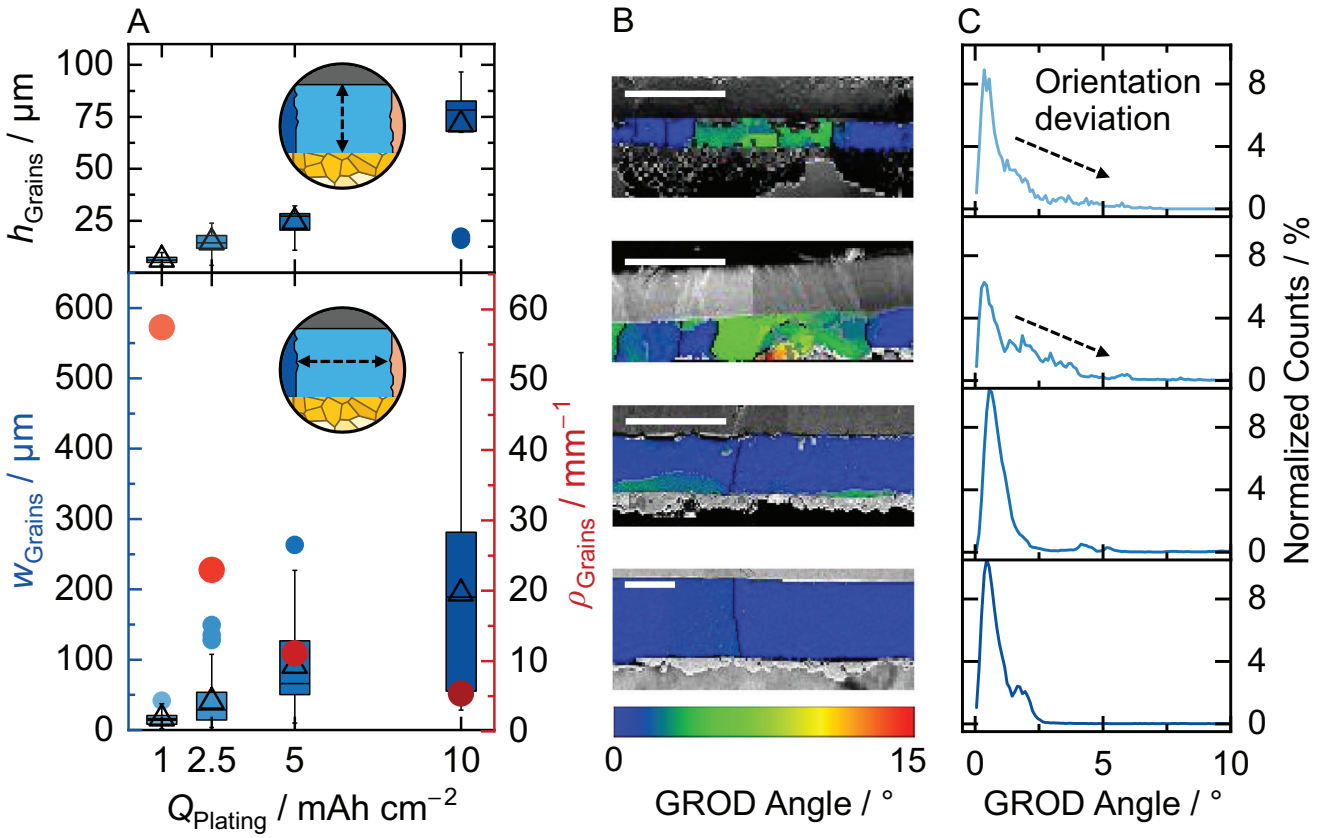

Figure 5. Summary of the analyzed lithium layers electrodeposited with different layer thicknesses. A) Boxplot of the analyzed lithium layers electrodeposited with 100 µA cm^{-2} for different capacities. The measured grain heights are summarized in the boxplot in black on the top graph. The measured grain widths are summarized in the boxplot in blue underneath. The dimension of interest for the respective boxplot is schematically depicted within the plot. Outliers (interquartile range factor = 1.5) are marked with blue points in both boxplots. The distribution of both grain heights and widths summarizes 59 (1 mAh cm^{-2}), 54 (2.5 mAh cm^{-2}), 21 (5 mAh cm^{-2}), and 16 (10 mAh cm^{-2}) measured grains, respectively. The average is represented with a triangle inside each box. The calculated grain density is shown in red circles in the lower section. B) Overlay of SEM images with GROD maps for the different layer thicknesses, see also Figures S14–S17 (Supporting Information). The shown scale bars correspond to 50 µm. Angular deviations of individual pixels referenced to the mean orientation of the grain are shown according to the color scale below. C) Distribution of the measured GROD angles for all analyzed grains. The data is normalized to the total counts. The drawn arrows highlight the shift toward higher GRODs for lower capacities.

grain growth is potentially further enhanced by the fact that a high-purity lithium layer is electrodeposited, given that Li_6PS_5Cl is a single-ion conductor – leading to the absence of impurities which would potentially hinder grain boundary motion.[1,4,53,54]

Additionally, a lowering of the local degrees of misorientation and the associated strain within the grains could be a reason for the change in microstructure. As can be seen in Figure 5, the distribution of GROD angles shifts toward smaller values for higher layer thicknesses. This means that fewer grains show high GROD angles in their interior. The mean GROD angle is 1.35° for Q = 1 mAh cm^{-2}, 1.78° for Q = 2.5 mAh cm^{-2}, 1.12° for Q = 5 mAh cm^{-2}, and 0.87° for Q = 10 mAh cm^{-2}. Only the experiment with Q = 1 mAh cm^{-2} deviates from the trend, which could be because no severe (lateral) grain growth has yet taken place. Also, the GROD maps (see Figure 5B; Figures S14–S17, Supporting Information) show that there appear to be more grains with high GROD angles at lower layer thicknesses. In particular, the layer for Q = 2.5 mAh cm^{-2} shows multiple grains with high GROD angles and subgrain structures in their interior. Such subgrain structures are suspected to favor abnormal grain growth.[45–49] Interestingly, Omori et al. found similar columnar structures within high-temperature processed copper alloys.[48] With increasing layer thickness, at Q = 5 mAh cm^{-2}, such misorientations can only be recognized sporadically, and at Q = 10 mAh cm^{-2} there are almost no more grains that show misorientation angles. We herein conclude that the electrodeposited layers reduce their stress during vertical growth, which could be another driving force for the lateral growth observed.

The observed grain growth is in agreement with molecular dynamics simulations of Choi et al.[55] and could potentially follow a normal grain growth mechanism described by Thompson,[49] leading to a columnar grain structure and grain diameters in the range of 2–4 times the layer thickness, following a lognormal distribution.[49] These assumptions fit well with the lithium grains analyzed here, as can be seen in the grain width distribution plot in Figures S18, S19 (Supporting Information). The grain size distribution for different current densities shows good agreement between the lognormal distribution and the experimental data, suggesting that normal grain growth has taken place. The same applies to the thicker lithium layer for Q = 2.5 mAh cm^{-2},

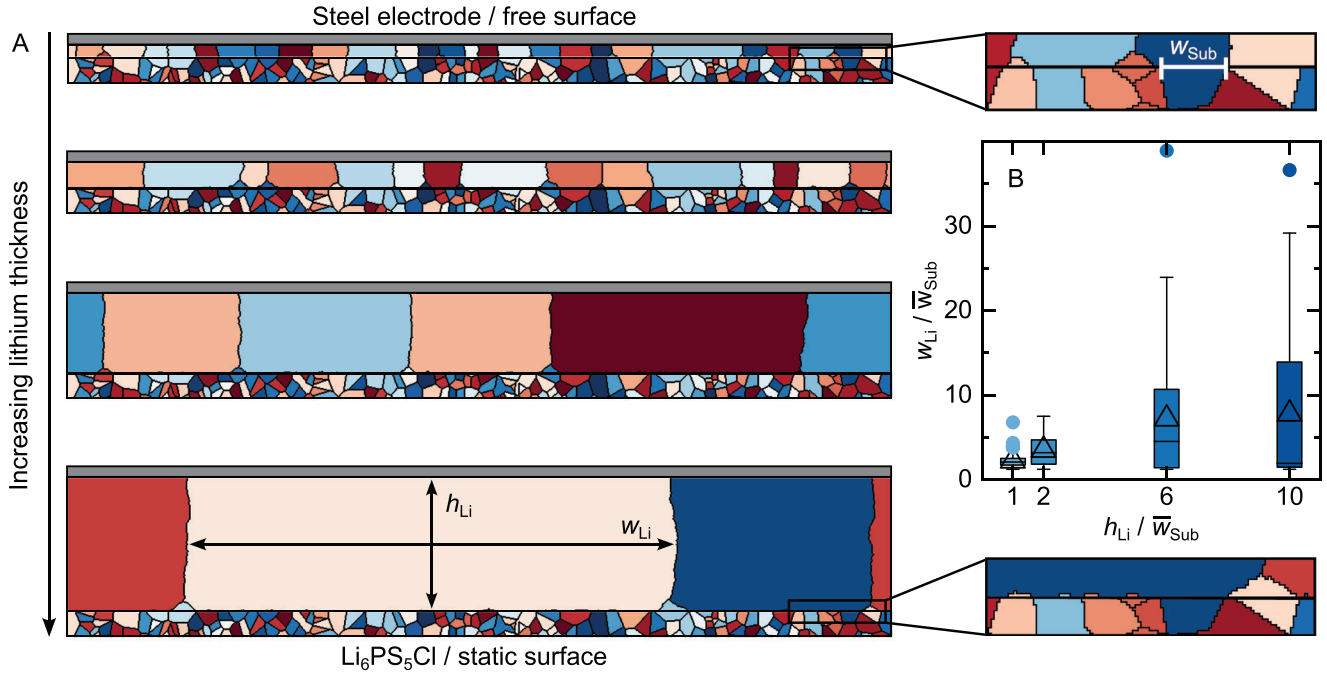

Figure 6. Simulation-based results on the microstructural evolution of lithium. A) Simulation-based microstructures of lithium layers of different thicknesses with a free surface toward the top (imitating steel foil) and a static interface toward the solid electrolyte at the bottom (imitating Li_6PS_5Cl). The two inlets on the right show an enlarged section of the Li|Li_6PS_5Cl interface. B) Boxplot of grain width w_{Li} versus lithium thickness h_{Li}. Both values are referenced to the average width of the Li_6PS_5Cl grains at the Li|Li_6PS_5Cl interface $\bar{w}_{Sub}$. The width of one Li_6PS_5Cl grain (w_{Sub}) is highlighted in the upper inlet as an example. For the boxplot, 5 structures, as shown in (A), were generated and analyzed for each of the different lithium thicknesses.

which also appears to be lognormally distributed. The continued growth of the grains for $Q = 5$ mAh cm^{-2} and 10 mAh cm^{-2} could either be due to the same mechanism or due to abnormal grain growth, which is described by both Thompson[49] and Omori et al.[48] Unavoidably, the quality of the statistics is reduced due to the decreasing number of grains for the thicker layers, which makes it difficult to draw more reliable conclusions. At this point, we like to note that the data presented here are the first of their kind and already require extensive analysis through a time-consuming workflow for the EBSD experiments on millimeter-sized cross-sections. More data will be generated in the future, including the role of other parameters like interface modification or seed layers.

2.4. Modelling of the Microstructural Evolution

To qualitatively describe the observed layer thickness dependence, a Monte Carlo Potts model is used in the following. Herein, we aim to model the microstructures for the different lithium layer thicknesses. To simulate the thickness dependence of the lithium microstructure after electrodeposition, the actual electrodeposition kinetics are disregarded. Instead, based on our previous results, we hypothesize that the lithium layer rapidly anneals during or after electrodeposition, as electrodeposition is conducted at a high homologous temperature of $T_H = 0.66$ for lithium. This hypothesis is supported by *operando* experiments of Fuchs and Ortmann et al.[39] Consequently, when observing the metal layer using SEM, a fully annealed, i.e., equilibrated lithium layer can be seen, with the microstructure primarily determined by the layer thickness d_{layer}. This approach aligns with our experimental findings, which show no significant differences in the microstructure based on the deposition rate (i.e., applied current density).

For each thickness, an identical Li_6PS_5Cl grain microstructure with the same spatial distribution of orientations ϑ_i and a free surface imitating the steel electrode is attached to the lithium layer (see **Figure 6**; Figure S20, Supporting Information). Random orientation values ϑ_i are assigned to the lithium Monte Carlo Units (MCUs). We then anneal the structure via 10^6 Monte Carlo time steps, leading to grain growth as shown in Figure S21 (Supporting Information). After these 10^6 steps, the total energy and mean grain size reaches an equilibrium state (see Figure S22, Supporting Information).

The final microstructures for different layer thicknesses are shown in Figure 6. The layer thicknesses are given in units of w_{Sub}, which is the mean (interface) diameter of the Li_6PS_5Cl grains at the Li|Li_6PS_5Cl interface. The color coding of the grains reflects their relative orientation ϑ_i, with low interfacial energies appearing between lithium and Li_6PS_5Cl grains of similar colors (e.g., light blue and blue, or light red and red).

As visible in Figure 6A, the simulation results in columnar grains with boundaries perpendicular to both the Li|Li_6PS_5Cl and the steel|Li interfaces. Additionally, at the Li|Li_6PS_5Cl interface, smaller truncated grains remain, primarily forming triple junctions with the larger columnar grains, being in good agreement with our experimental data. The relative orientations ϑ_i of these smaller grains match those of the adjacent Li_6PS_5Cl grains,

resulting in low interfacial energies. For small layer thicknesses, the lithium layer's grain orientation adopts the orientation of the adjacent SE grains.

In contrast, none of these truncated grains is visible at the upper interface toward the steel foil, which was modeled as a free surface. Comparing simulation and experiment, this highlights the necessity of introducing an interface interaction at the Li|Li_6PS_5Cl boundary to qualitatively reproduce our experimental results. However, it is important to note that SEI formation takes place at the Li|Li_6PS_5Cl interface. Therefore, rather the SEI will influence the lithium microstructure instead of the Li_6PS_5Cl itself. Nevertheless, it seems evident that the lithium microstructure is influenced by the interaction at the interface towards the Li_6PS_5Cl. Our simulations further indicate that these effects are more pronounced for thinner lithium layers. This is because the relative contribution of $\gamma_{i,j}^{\mathrm{int}}$ to E_{tot} becomes more significant, given the increasing ratio between interfacial area and grain boundary area. This forces the lithium adjacent to the Li_6PS_5Cl surface to favor crystal orientations with low interface energies (epitaxial growth). Conversely, the contribution of $\gamma_{i,j}^{\mathrm{gb}}$ to E_{tot} becomes more significant for thicker grown layers, as the total grain boundary area increases in the course of electrodeposition, unlike the interfacial area with the substrate.

The mean width w_{Li} of columnar grains increases with increasing lithium layer thickness, as can be seen both in the generated structures in Figure 6A as well as in the boxplot in Figure 6B. Please note that only grains with a minimum width of 15 pixels were considered for the boxplot. This ensures that the analyzed grains are not artifacts of the simulation, e.g. grains that only consist of single pixels. Although no electrodeposition kinetics were considered in the model, the results are in qualitative agreement with the experiment, suggesting that the layer thickness is decisive for the resulting microstructure and that the observed layers are equilibrated. The underlying physics for the increasing grain width of the columnar grains is as follows: grains grow curvature-driven until their size matches the layer thickness. The driving force is the reduction of the total grain boundary area, associated with higher free energy of the layer. Then stagnation of the grain growth occurs (see Figure S22, Supporting Information) as the curvature of the grain boundaries approaches zero, eliminating the driving force for further growth. This leads to a linear relationship between grain width and layer thickness, as demonstrated by simulations on grain growth by Zöllner and experimental observations on thin layers.[56–59] As shown in Figure 6, this linear relationship holds for the columnar grains in our simulation.

The simulations reveal that the experimental results can be qualitatively reproduced without taking electrodeposition kinetics into account, supporting the hypothesis that deposition rate (i.e., the current density) has no significant influence on the resulting microstructure. We conclude that the lithium layer anneals rapidly during or after electrodeposition in dependence on the lithium layer thickness. Furthermore, by implementing an interfacial energy between lithium and Li_6PS_5Cl, we induced the formation of truncated grains in the simulation. These truncated grains only occur at this interface and not on the side of the steel foil, both in the simulation and in the experiment. Thus, our hypothesis that the steel foil does not significantly influence the lithium microstructure is supported, but an influence of the Li_6PS_5Cl microstructure on the lithium microstructure is obvious. However, we would like to point out that the choice of other current collector materials might lead to a different outcome.

What remains an open question is the stagnating grain growth in 3D. Here, grain growth should slow down but not stop when the grain diameter matches the layer thickness due to residual boundary curvature. Possible explanations include the extremely slow coarsening of low-curvature grains, making the study's timeframe too short to observe changes. Surface grooving and rough interface topology might also pin grain boundaries, similar to 2D mechanisms.[60] Additionally, orientation-dependent interface energies could lead to triangular grains that pin columnar grain boundaries at the SE|lithium interface. Further analysis is needed to understand the full effects of these factors, which may reveal additional insights.

2.5. Microstructural Evolution During Lithium Electrodeposition

In the following, the observed microstructural evolution is discussed. The scheme in **Figure 7** serves as a schematic visualization of the conclusions drawn from the results presented above. The voltage profile in Figure 7A sketches lithium electrodeposition with two different current densities j_{low} and j_{high}. The small offset between the two curves only serves for better differentiation of the two. Initially, a nucleation overvoltage is visible for both current densities (point Q_0). Comparing (B) and (C), we assume that at higher current density (C) more nuclei are formed initially at the interface between steel and Li_6PS_5Cl, as has been demonstrated previously for RFCs.[22,31]

During continuous electrodeposition (point $Q_1 > Q_0$), those nuclei grow and become grains. Because nuclei can have the same orientation, some nuclei grow together to form a single grain. At this point, grain growth occurs mostly in a vertical direction. A lateral grain growth before complete coverage of the solid electrolyte surface might be due to current constriction at the edge of the lithium grains. In addition, mechanical stress could also favor lateral growth. At this early stage of growth, the higher nucleation density for j_{high} may still result in a higher grain density compared to the lower current density j_{low}, as no significant grain growth has yet happened in both vertical and lateral directions. As shown schematically, however, we assume that misorientations and substructures already form within the grains, especially at contact points between two neighboring grains. Based on our simulations, we further assume that during this initial stage, the microstructure of lithium adopts the microstructure of the SE.

At higher electrodeposition capacity (point $Q_2 > Q_1$), we observe a harmonization of the microstructure, which means that – despite different nucleation densities – the same number of grains with a similar size is now present in both cases. We assume that a curvature-driven normal grain growth together with the reduction of misorientations inside the grains is the driving force, being schematically indicated by a reduction of highly misoriented regions in Figures 7B,C.[46–49]

This effect is even more pronounced with longer electrodeposition (point $Q_3 > Q_2$). Existing grains further grow, increasing the average grain size and decreasing the grain density, also decreasing the surface-to-volume ratio of the remaining grains.

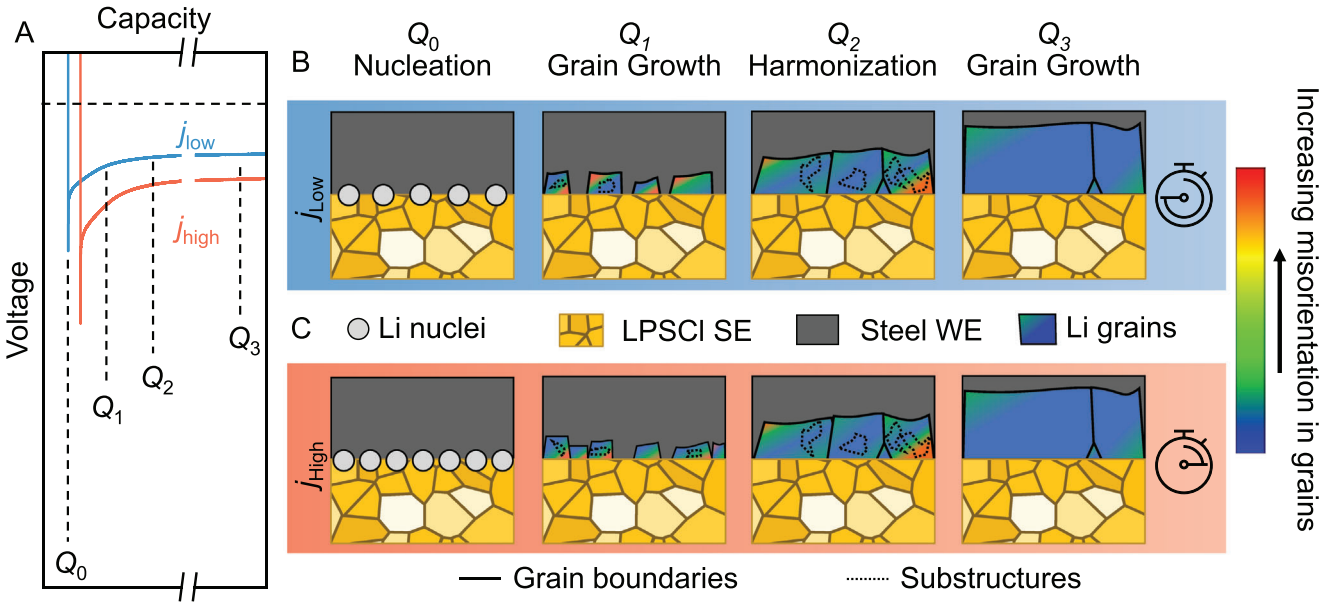

Figure 7. Schematic representation of the microstructural evolution of electrodeposited lithium. A) Sketch of voltage profiles for two different current densities j_{low} and j_{high}. The capacity-offset between the two curves serves for better differentiation. B, C) Microstructural evolution during electrodeposition of lithium for (B) j_{low} and (C) j_{high}. Please note that, as indicated by the stopwatches, electrodepositing the same capacity Q with a lower current density $j_{low} < j_{high}$ takes longer. The color code within the grains highlights misorientation, according to the color scale on the right of the image. Dotted lines indicate substructures that form within grains.

This leads to very large lateral grain sizes in the range of several hundred micrometers and some truncated grains, as visible in the analyzed layers within this work. Additionally, we found that the misorientation within grains further decreases for higher layer thickness, as indicated by a more homogeneous color gradient in Figure 7 at point Q_3.

Based on our results and the work of Thompson, and Omori et al., we assume that the truncated grains are not caused by different growth rates of the grains.[48,49] Instead, we assume that they are either caused by the fusion of neighboring grains, which is driven by the reduction of misorientations, or due to an interfacial interaction with the solid electrolyte, as indicated by our simulations. It remains elusive whether these truncated grains are formed at the beginning or during electrodeposition.

One possible mechanism for the observed grain growth is a curvature-driven normal grain growth. As postulated by Thompson,[49] normal grain growth occurs in thin layers with grain sizes smaller than the layer thickness until the resulting columnar grains span the whole layer and grain sizes are in the order of the layer thickness, being referred to as a specimen thickness effect. This is in good agreement with both our experimental and computational results, indicating a similar grain growth mechanism. Additionally, as mentioned during the discussion of Figure 5, room temperature corresponds to a homologous temperature of $T_H = 0.66$ for lithium metal, making grain growth more likely due to a presumably high grain boundary mobility.

Furthermore, "secondary recrystallization" or abnormal grain growth could take place. Here a few grains grow preferentially at the expense of other surrounding grains.[39,49] Abnormal grain growth has been observed in tantalum, molybdenum, and copper alloys, for example.[46,48,61] In the case of copper alloys, a cyclic temperature treatment causes the formation of substructures and high GROD angles.[48] These in turn are suspected to be the origin of abnormal grain growth, leading to grain sizes in the millimeter range and, interestingly, also to a columnar structure. As discussed, such misorientations are also visible within electrodeposited lithium layers, as schematically depicted in Figure 7, or using GROD angle measurements (see Figure 5B; Figures S14–17, Supporting Information), potentially initiating abnormal grain growth here, too. In the case of abnormal grain growth, a preferential orientation of the abnormally grown grains is expected.[49] An analysis of the thickest lithium layer (revisit Figure S10, Supporting Information) shows that the largest grains have a similar <111> orientation in the *y*-direction (blue), potentially caused by abnormal grain growth. For direct visualization of the orientation distribution, the inverse pole figure of this layer is shown in Figure S23 (Supporting Information). The thinner lithium layers are also shown for comparison. However, the large grain size for $Q = 10$ mAh cm^{-2} and thus poorer statistics on the one hand and the observation of the completely annealed state on the other hand makes it difficult to draw reliable conclusions on preferential growth. A deeper understanding of the detailed growth mechanisms is to be gathered in future studies, combining additional *operando* measurements, complemented by EBSD analysis.

Overall, we demonstrate that the microstructure of electrodeposited lithium can be controlled by varying the layer thickness. By decreasing the electrodeposition capacity (i.e., the layer thickness), a smaller grain size with a higher grain density can be electrodeposited. Assuming faster lithium diffusion along the grain boundaries, a higher power density can be achieved for small layer thicknesses. Furthermore, the microstructure differs significantly from that of commercially available foils, not only due to the reduced grain size of electrodeposited lithium layers

with practically relevant thicknesses of 20 µm (also resulting in a higher grain boundary density) but also because of the columnar structure of the layer. Both parameters likely influence the re-dissolvable amount of the lithium layer during cycling. In addition to electrochemical properties, mechanical properties are also determined by the microstructure. Assuming a Hall–Petch mechanism (i.e., grain boundary strengthening), it can be expected that thinner lithium layers are harder than thicker lithium layers, as the grain boundary density is inversely proportional to the layer thickness.[52] Finally, the model system presented here enables further investigations of the lithium microstructure and how it can be influenced. Possible approaches include varying the temperature during electrodeposition or the use of seed layers, which could influence nucleation and grain growth.

3. Conclusions

In this study, we experimentally investigated the microstructure of electrodeposited pure lithium as a function of the current density and the electrodeposited layer thickness at steel|Li_6PS_5Cl interfaces using EBSD. Our experiments show that the steel|Li_6PS_5Cl|Li|steel cell setup is a suitable model system for RFCs, enabling the electrodeposition of lithium layers with a thickness of several tens of micrometers.

Varying the current density used for lithium electrodeposition does not influence the microstructure for the analyzed layer thicknesses of ≈5 µm of lithium. Despite an assumed higher nucleation density at higher current densities, the average grain size and density remain similar. Instead, the microstructure depends on layer thickness. For thicker layers, the lateral grain size increases, too. Thus, we conclude that – although the current density plays an important role in the morphology of electrodeposited lithium layers – its effect on the microstructure is overshadowed by grain growth during electrodeposition of practically relevant lithium layer thicknesses. This specimen thickness effect is further supported by our simulations based on a Monte Carlo Potts model, which qualitatively reproduces our experimental results without taking electrodeposition kinetics into account. In accordance with previous work, thinner electrodeposited lithium layers should therefore show a higher Coulomb efficiency (i.e., the amount of re-dissolvable lithium is higher) under equal current load, as the transport of lithium along grain boundaries is assumed to be faster.[18,39,62]

Accordingly, particular attention should be paid to the choice of lithium layer thickness, as it significantly influences the resulting lithium microstructure and the electrochemical properties for subsequent investigations. To achieve higher power densities in practice, it might be better to stack several thin single cells rather than trying to develop thick cells with high areal capacity. In conclusion, our work provides a deeper understanding of electrodeposited lithium and its properties. Its microstructure is related to electrodeposition parameters, offering the perspective to be modified in future work to increase the amount of re-dissolvable lithium during cycling experiments.

4. Experimental Section

Cell Preparation: RFC (steel|Li_6PS_5Cl|Li|steel) preparation was carried out inside a glovebox (MBraun, Germany) with impurity contents of O_2, N_2 and H_2O being below 1 ppm. An in-house casing was used for cell assembly. Steel stamps with a diameter of 10 mm were used to contact the electrodes. One of the steel pistons was fixed with the help of nitrile rubber sealing rings as well as polyether ether ketone cell components. A steel foil (AISI 304, Goodfellow, Germany) acting as the working electrode was placed on the fixed steel punch and 90 mg of Li_6PS_5Cl powder (NEI Corporation, USA) was filled in. The other opening of the cell housing was similarly sealed with a second steel punch to compress the SE and the powder was compacted using a uniaxial press at 3 t for 1 min from each side, resulting in a pellet with a thickness of roughly 1 mm. Lithium foil was freshly prepared by cutting a small piece of lithium from a lithium rod (99.8%, abcr GmbH) and removing the surface degradation layers by mechanical removal using a ceramic knife. The fresh piece of lithium was then pressed between a pouch foil to form a clean lithium foil with a thickness of ≈100 µm using a hand press.[10] A lithium electrode (d = 9 mm) was punched out and placed on the remaining surface (opposite to the steel working electrode) of the Li_6PS_5Cl pellet. An additional steel foil was placed between the steel punch and the lithium electrode. Finally, the cell was sealed and a stack pressure of 15 MPa was applied using an aluminum press frame for electrochemical characterization.

Electrochemical Characterization: The cells were electrochemically characterized using a VMP 300 potentiostat (Biologic, France) at room-temperature (25 °C). Initially, the cells were equilibrated for ≈6 h, and potentiostatic impedance spectra were recorded in a frequency range from 7 MHz to 100 MHz at an amplitude of 10 mV at an interval of 30 min. Subsequently, lithium was electrodeposited on the working electrode by galvanostatic electrochemical impedance spectroscopy (GEIS) using different current densities (50 µA cm^{-2}, 100 µA cm^{-2}, 250 µA cm^{-2}, and 500 µA cm^{-2}). For thickness-dependent measurements, the capacity was limited to 1 mAh cm^{-2}, 2.5 mAh cm^{-2}, 5 mAh cm^{-2}, and 10 mAh cm^{-2} while the current density was kept constant at 100 µA cm^{-2}. Unless otherwise stated, GEIS measurements were recorded with a frequency range from 7 MHz to 1 Hz at an amplitude of 10% of the direct current.

Cryogenic Ion Milling: For the preparation of cross-sections an ion beams milling system (Leica EM TIC 3X, Leica Microsystems GmbH, Germany) at temperatures below −100 °C was used in combination with a Leica VCT500 (Leica Microsystems GmbH, Germany) transfer module. An accelerating voltage of 6 kV, resulting in an Ar^+ ion beam current of ≈2.2 mA was used to cut steel|Li cross-sections. Cross-sections were imaged using a field-emission scanning electron microscope GeminiSEM 560 system (SEM, Carl Zeiss Microscopy GmbH, Germany).

Electron Backscatter Diffraction (EBSD): For EBSD measurements, the sample was transferred into the SEM using an inert-transfer module (Leica VCT500, Leica Microsystems GmbH, Germany). Microstructural analysis was conducted at a beam voltage of 10 kV, a beam current of ≈12 nA, a working distance of 12.5 mm, and a tilt of 70° using an EBSD detector system (Symmetry S3) from Oxford Instruments (Oxford Instruments, United Kingdom).

Data Processing and Analysis: Acquired EBSD data were processed with the AZtecCrystal software from Oxford Instruments and the implemented Mapsweeper software package. The acquired electron backscatter patterns were indexed using a Hough algorithm with a resolution of 60 and 11 bands considering the cubic Li ($Im\bar{3}m$) phase. Dynamical template matching, refinement sweeps, and repair sweeps were executed against a master simulation of EBSD patterns of lithium to refine the measured patterns and remove artifacts such as pseudo-symmetries within grains. The grain reference orientation deviation (GROD) angle was calculated within AZtec Crystal. For this, the mean grain orientation was calculated by using every measured pixel of a grain. The angular deviation of the individual pixels were then referenced to the calculated mean value.

Grain Growth Simulations: The grain growth simulations were carried out using a Monte Carlo Potts Model, frequently used to simulate curvature-driven grain growth.[56–59,63–69] In the model, the microstructure of the lithium metal was mapped onto a square lattice. Each lattice site is

called a Monte Carlo unit (MCU) and is assigned a state that corresponds to the particular grain orientation of the grain to which the lattice site belongs to. This means that grain boundaries were implicitly assigned to the boundary between two adjacent MCUs i and j with different orientations (see Figure S20, Supporting Information). The grain boundary energy per unit length $\gamma_{i,j}^{gb}$ in such models is typically assumed to follow the Read–Shockley-equation:

$$\gamma_{i,j}^{gb} = \begin{cases} \gamma_{max}^{gb} \frac{\theta_{i,j}^{gb}}{\theta^{gb*}} \left(1 - \ln\left(\frac{\theta_{i,j}^{gb}}{\theta^{gb*}}\right)\right) \text{ if } \theta_{i,j}^{gb} \leq \theta^{gb*} \\ \gamma_{max}^{gb} \text{ if } \theta_{i,j}^{gb} > \theta^{gb*} \end{cases} \quad (1)$$

Here, $\theta_{i,j}^{gb}$ represents the crystallographic misorientation angle between the neighboring lattice sites i and j, while θ^{gb*} denotes the critical misorientation angle that distinguishes small-angle grain boundaries from large-angle grain boundaries. This means that all grain boundaries with $\theta_{i,j} \geq \theta^*$ exhibit the maximum grain boundary energy γ_{max}^{gb}. In the analysis, this orientation dependence of $\gamma_{i,j}^{gb}$ was neglected for the interior of the lithium and thus only assume large angle grain boundaries ($\gamma_{i,j}^{gb} = \gamma_{max}^{gb}$). This assumption leads to a grain size evolution that closely approximates ideal grain growth, with the mean grain diameter following a square root time dependence (see Figure S21, Supporting Information). In such cases, grain growth was driven only by the local curvature κ of the grain boundary, i.e., the local grain boundary velocity v toward its center of curvature was proportional to κ.

To account for the potential influence of the SE, a polycrystalline layer was attached to one side of the lithium layer. This layer remains static during the simulation, with its MCUs defining the (static) boundary conditions on the SE side of the lithium layer (revisit Figure S20, Supporting Information). In contrast to $\gamma_{i,j}^{gb}$, it was assumed that the interfacial energy $\gamma_{i,j}^{int}$ between a lithium MCU i and an adjacent SE MCU j follows Equation 1. Specifically, $\gamma_{i,j}^{int}$ was calculated using the maximum interfacial energy γ_{max}^{int} and an effective misorientation angle $\theta_{i,j}^{int}$ that separates high energetic relative orientations of the SE MCUs and the lithium MCUs from low-energetic ones.

In 3D space, $\theta_{i,j}^{int}$ is likely a complex function of the orientations (Euler angles) of the SE grains and their adjacent lithium grains. However, for a qualitative understanding of the experimental observations, a simplified approach similar to that of Zöllner et al. used for the calculation of grain boundary misorientations was adopted.[67] In this approach, each lithium and SE MCU was assigned a relative misorientation $\vartheta_i (\vartheta_i \in \mathbb{N}; \vartheta_i \leq 45)$ with respect to a reference axis, and $\theta_{i,j}^{int}$ was calculated according to:

$$\theta_{i,j}^{int} = \left|\vartheta_i - \vartheta_j\right| \quad (2)$$

Given the lack of quantitative information on γ_{max}^{int}, it was assumed to be equal to γ_{max}^{gb}.

Due to the significantly smaller grain size of the steel foil compared to that of the deposited lithium layer (revisit Figure S6, Supporting Information), an isotropic interaction was assumed at the steel|Li interface. For simplicity, the attached steel electrode was modeled as a free surface with $\gamma_{i,j}^{int} = 0$ between all lithium MCUs i and adjacent steel MCU j. For the boundaries perpendicular to the SE surface normal, periodic boundary conditions were applied, meaning that the nearest neighbor of an MCU at the edge of the lattice was the corresponding MCU on the other edge, and vice versa (see Figure S20, Supporting Information).

The total energy of the system E_{tot}, excluding contributions from the interior of the SE and steel layer, was given by summing up the energetic contributions of all N lithium lattice sites. Here, only interactions of each lattice side with their 8 nearest neighbors (nn) were considered. Lattice sites with the same ϑ_i do not contribute to E_{tot}. Consequently, it was given as:

$$E_{tot} = \frac{1}{2} \sum_{i=1}^{N} \sum_{j=1}^{nn} \left(\gamma_{max}^{gb} + \gamma_{i,j}^{int}\right) \left(1 - \delta\left(\vartheta_i, \vartheta_j\right)\right) \quad (3)$$

Here, $\delta(\vartheta_i, \vartheta_j)$ is the Kronecker-delta which is equal to one if $\vartheta_i = \vartheta_j$ and zero if $\vartheta_i \neq \vartheta_j$. Obviously $\gamma_{i,j}^{int} = 0$ for the lithium MCUs that are not in contact with the SE boundary units.

To update the orientations of the lithium MCUs, i.e., anneal the lithium, a Monte Carlo simulation was carried out. The corresponding algorithm works as follows: an MCU was chosen in a probabilistic way and its ϑ_i was changed to one of its 8 nearest neighbor states ϑ_j. Choosing the orientation only from neighbor states prevents the nucleation of new grains. A new ϑ_i was accepted with a probability P according to:

$$P = \begin{cases} 1 \text{ if } \Delta E_{tot} \leq 0 \\ exp\left(-\Delta E_{tot}/k_b T_s\right) \text{ if } \Delta E_{tot} > 0 \end{cases} \quad (4)$$

where ΔE_{tot} is the energy difference between the old and the new lattice state calculated based on Equation 3, k_b is the Boltzmann constant, and T_s the simulation temperature. T_s is a technical parameter and should not be confused with a real temperature.[68] The proposal by Zöllner was followed and $k_b T_s$ was chosen to be equal to $0.66 \bullet \gamma_{max}^{gb}$. A repetition of N reorientation attempts defines the time scale of the simulation, equivalent to one Monte Carlo step (MCS). The simulation was carried out in a parallel fashion by dividing the grid into four subunits with non-interacting MCUs.[70] Consequently, four iterations were needed for N reorientation attempts, i.e., to perform one MCS. All simulation steps were carried out using Python.

It is important to note here that, strictly speaking, neither the time scale, the size scale, nor the energy scale of this model directly corresponds to the actual physical quantities of the experiments. Various methods have been proposed in the literature, such as those by Raabe,[71] to translate the Monte Carlo parameters into real physical units. However, since the experimental results do not provide quantitative data on the grain growth kinetics of the lithium layers, such methods cannot be applied here.

Supporting Information

Supporting Information is available from the Wiley Online Library or from the author.

Acknowledgements

The authors thank Pascal Becker for assistance in cell preparation. S.K. acknowledges fruitful discussions with Dr. Habil. Dana Zöllner (Otto von Guericke University, Magdeburg, Germany) on Monte Carlo Potts simulations. The authors acknowledge the fruitful discussion with Prof. Dr.-Ing. Habil. Dierk Raabe (Max-Planck-Institut für nachhaltige Materialien GmbH) on metal microstructure. The authors (J.J., J.B.) acknowledge funding by Evonik Operations GmbH, as well as by the German Research Foundation (DFG) under Project ID 390874152 (POLiS Cluster of Excellence). This work had been partly funded by the German Federal Ministry of Education and Research (BMBF) within the DE-US program under the project "LiSI2", grant identifier 03XP0509B.

Open access funding enabled and organized by Projekt DEAL.

Conflict of Interest

The authors declare no conflict of interest.

Author Contributions

J.B. did conceptualization, methodology, investigation, validation, formal analysis, wrote the original draft, visualization, and did review & editing. T.F. did conceptualization, methodology, and did review & editing. T.O. did conceptualization, methodology, did review & editing. S.K. performed formal analysis, software, visualization, did review & editing. F.H.R. wrote the original draft, did review & editing, supervision. J.J. did conceptualization, methodology, resources, supervision, wrote the original draft, did review & editing, and funding acquisition.

Data Availability Statement

The data that support the findings of this study are available from the corresponding author upon reasonable request.

Keywords

anode-free cells, electron backscatter diffraction, lithium metal, microstructure, solid-state battery

Received: October 25, 2024
Revised: November 25, 2024
Published online:

[1] J. Janek, W. G. Zeier, *Nat. Energy* **2016**, *1*, 16141.
[2] S. Randau, D. A. Weber, O. Kötz, R. Koerver, P. Braun, A. Weber, E. Ivers-Tiffée, T. Adermann, J. Kulisch, W. G. Zeier, F. H. Richter, J. Janek, *Nat. Energy* **2020**, *5*, 259.
[3] T. Krauskopf, F. H. Richter, W. G. Zeier, J. Janek, *Chem. Rev.* **2020**, *120*, 7745.
[4] B. S. Vishnugopi, E. Kazyak, J. A. Lewis, J. Nanda, M. T. McDowell, N. P. Dasgupta, P. P. Mukherjee, *ACS Energy Lett.* **2021**, *6*, 3734.
[5] P. Albertus, S. Babinec, S. Litzelman, A. Newman, *Nat. Energy* **2018**, *3*, 16.
[6] S. K. Otto, Y. Moryson, T. Krauskopf, K. Peppler, J. Sann, J. Janek, A. Henss, *Chem. Mater.* **2021**, *33*, 859.
[7] B. Aktekin, L. M. Riegger, S. K. Otto, T. Fuchs, A. Henss, J. S. E. I. Janek, *Nat. Commun.* **2023**, *14*, 6946.
[8] L. M. Riegger, S. Mittelsdorf, T. Fuchs, R. Rueß, F. H. Richter, J. Janek, *Chem. Mater.* **2023**, *35*, 5091.
[9] S. K. Otto, L. M. Riegger, T. Fuchs, S. Kayser, P. Schweitzer, S. Burkhardt, A. Henss, J. I. Janek, *Adv. Mater. Interfaces* **2022**, *9*, 2102387.
[10] T. Krauskopf, H. Hartmann, W. G. Zeier, J. Janek, *ACS Appl. Mater. Interfaces* **2019**, *11*, 14463.
[11] M. J. Wang, E. Carmona, A. Gupta, P. Albertus, J. Sakamoto, *Nat. Commun.* **2020**, *11*, 6400.
[12] Y.-G. Lee, S. Fujiki, C. Jung, N. Suzuki, N. Yashiro, R. Omoda, D.-S. Ko, T. Shiratsuchi, T. Sugimoto, S. Ryu, J. H. Ku, T. Watanabe, Y. Park, Y. Aihara, D. Im, I. T. Han, *Nat. Energy* **2020**, *5*, 299.
[13] D. Spencer-Jolly, V. Agarwal, C. Doerrer, B. Hu, S. Zhang, D. L. R. Melvin, H. Gao, X. Gao, P. Adamson, O. V. Magdysyuk, P. S. Grant, R. A. House, P. G. Bruce, *Joule* **2023**, *7*, 503.
[14] J. Betz, G. Bieker, P. Meister, T. Placke, M. Winter, R. Schmuch, *Adv. Energy Mater.* **2019**, *9*, 1803170.
[15] B. Xu, D. Qian, Z. Wang, Y. S. Meng, *Mater. Sci. Eng. R: Rep.* **2012**, *73*, 51.
[16] A. J. Sanchez, N. P. Dasgupta, *J. Am. Chem. Soc.* **2024**, *146*, 4282.
[17] D. K. Singh, T. Fuchs, C. Krempaszky, P. Schweitzer, C. Lerch, F. H. Richter, J. Janek, *Matter* **2023**, *6*, 1463.
[18] D. K. Singh, T. Fuchs, C. Krempaszky, B. Mogwitz, S. Burkhardt, F. H. Richter, J. Janek, *Adv. Funct. Mater.* **2023**, *33*, 2211067.
[19] J. Aspinall, D. E. J. Armstrong, M. Pasta, *Mater. Today Energy* **2022**, *30*, 101183.
[20] S. E. Sandoval, M. T. McDowell, *Matter.* **2023**, *6*, 2101.
[21] H. Somekawa, K. Nishikawa, T. Moronaga, T. Ohmura, *J. Power Sources* **2023**, *569*, 233019.
[22] T. Fuchs, J. Becker, C. G. Haslam, C. Lerch, J. Sakamoto, F. H. Richter, J. Janek, *Adv. Energy Mater.* **2023**, *13*, 2203174.
[23] P. Arora, R. E. White, M. Doyle, *J. Electrochem. Soc.* **1998**, *145*, 3647.
[24] B. Aktekin, M. J. Lacey, T. Nordh, R. Younesi, C. Tengstedt, W. Zipprich, D. Brandell, K. Edström, *J. Phys. Chem. C* **2018**, *122*, 11234.
[25] A. Tornheim, D. C. O'Hanlon, *J. Electrochem. Soc.* **2020**, *167*, 110520.
[26] E. Kazyak, M. J. Wang, K. Lee, S. Yadavalli, A. J. Sanchez, M. D. Thouless, J. Sakamoto, N. P. Dasgupta, *Matter* **2022**, *5*, 3912.
[27] E. Kazyak, R. Garcia-Mendez, W. S. LePage, A. Sharafi, A. L. Davis, A. J. Sanchez, K. H. Chen, C. Haslam, J. Sakamoto, N. P. L. Dasgupta, *Matter* **2020**, *2*, 1025.
[28] L. E. Marbella, S. Zekoll, J. Kasemchainan, S. P. Emge, P. G. Bruce, C. P. Grey, *Chem. Mater.* **2019**, *31*, 2762.
[29] Y. Tang, L. Zhang, J. Chen, H. Sun, T. Yang, Q. Liu, Q. Huang, T. Zhu, J. Huang, *Energy Environ. Sci.* **2021**, *14*, 602.
[30] Q. Li, T. Yi, Wang, X., Pan, H., Quan, B., Liang, T., Guo, X., Yu, X., Wang, H., Huang, X., Chen, L., Li, *Nano Energy* **2019**, *63*, 103895.
[31] M. Motoyama, M. Hirota, T. Yamamoto, Y. Iriyama, *ACS Appl. Mater. Interfaces* **2020**, *12*, 38045.
[32] A. Pei, G. Zheng, F. Shi, Y. Li, Y. Cui, *Nano Lett.* **2017**, *17*, 1132.
[33] P. Bai, J. Li, F. R. Brushett, M. Z. Bazant, *Energy Environ. Sci.* **2016**, *9*, 3221.
[34] F. Shi, A. Pei, A. Vailionis, J. Xie, B. Liu, J. Zhao, Y. Gong, Y. Cui, *Proc. Natl. Acad. Sci. U S A* **2017**, *114*, 12138.
[35] J. Aspinall, K. Sada, H. Guo, S. Kotakadi, S. Narayanan, Y. Chart, B. Jagger, E. Milan, L. Brassart, D. Armstrong, M. Pasta, *Nat. Commun.* **2024**, *15*, 4511.
[36] Y.-J. Kim, S. H. Kwon, H. Noh, S. Yuk, H. Lee, H. Jin, J. Lee, J.-G. Zhang, S. G. Lee, H. Guim, H.-T Kim, *Energy Storage Mater.* **2019**, *19*, 154.
[37] Y. Hayashi, H. Miyazawa, K. Minamitani, I. Shohji, *Mater. Trans.* **2016**, *57*, 815.
[38] N. Brodusch, K. Zaghib, R. Gauvin, *Microsc. Res. Tech.* **2015**, *78*, 30.
[39] T. Fuchs, T. Ortmann, J. Becker, C. G. Haslam, M. Ziegler, V. K. Singh, M. Rohnke, B. Mogwitz, K. Peppler, L. F. Nazar, J. Sakamoto, J. Janek, *Nat. Mater.* **2024**, *23*, 1678.
[40] G. T. Lui, D. Chen, J. C. Kuo, *J. Phys. D Appl. Phys.* **2009**, *42*, 215410.
[41] A. Bastos, S. Zaefferer, D. Raabe, C. Schuh, *Acta Mater.* **2006**, *54*, 2451.
[42] M. J. Wang, R. Choudhury, J. Sakamoto, *Joule* **2019**, *3*, 2165.
[43] R. Weber, M. Genovese, A. J. Louli, S. Hames, C. Martin, I. G. Hill, J. R. Dahn, *Nat. Energy* **2019**, *4*, 683.
[44] H. Okamoto, *J. Phase Equilib. Diffus.* **2011**, *32*, 172.
[45] J. Ciulik, E. M. Taleff, *Scr. Mater.* **2009**, *61*, 895.
[46] E. M. Taleff, N. A. Pedrazas, *Science* **2013**, *341*, 1461.
[47] C. Lauhoff, T. Pham, A. Paulsen, P. Krooß, J. Frenzel, G. Eggeler, T. Niendorf, *Metal. Mater. Trans. A* **2022**, *53*, 4139.
[48] T. Omori, T. Kusama, S. Kawata, I. Ohnuma, Y. Sutou, Y. Araki, K. Ishida, R. Kainuma, *Science* **2013**, *341*, 1500.
[49] C. V. Thompson, *Annu. Rev. Mater. Sci.* **1990**, *20*, 245.
[50] P. W. Voorhees, *J. Stat. Phys.* **1985**, *38*, 231.
[51] W. Ostwald, *Z. für Phys. Chem.* **1900**, *34U*, 495.
[52] W. D. Callister, D. G. Rethwisch, in *Materials Science and Engineering: An Introduction*, 8th ed., John Wiley & Sons, Hoboken, NJ, USA **2009**.
[53] M. A. Kraft, S. P. Culver, M. Calderon, F. Böcher, T. Krauskopf, A. Senyshyn, C. Dietrich, A. Zevalkink, J. Janek, W. G. Zeier, *J. Am. Chem. Soc.* **2017**, *139*, 10909.
[54] P. A. Manohar, M. Ferry, T. Chandra, *ISIJ Int.* **1998**, *38*, 913.

[55] G. Choi, Y. Kim, J. Choi, D. Kim, *Adv. Energy Mater.* **2022**, *12*, 2201428.
[56] D. Zöllner, *Comput. Mater. Sci.* **2021**, *200*, 110803.
[57] D. Zöllner, *Comput. Mater. Sci.* **2016**, *125*, 51.
[58] D. Zöllner, W. Pantleon, *J. Phys.: Conf. Ser.* **2023**, *2635*, 012033.
[59] D. Zöllner, *Model. Simul. Mater. Sci. Eng.* **2024**, *32*, 035023.
[60] W. W. Mullins, *Acta Metall.* **1958**, *6*, 414.
[61] D. L. Worthington, N. A. Pedrazas, P. J. Noell, E. M. Taleff, *Metall. Mater. Trans. A* **2013**, *44*, 5025.
[62] J. S. Yoon, H. Sulaimon, D. J. Siegel, *J. Mater. Chem. A Mater.* **2023**, *11*, 23288.
[63] S. H. Oh, Y. J. Jeong, S. H. Na, J. Kim, B. J. Lee, *Acta Mater.* **2024**, *263*, 119542.
[64] A. J. Francis, C. G. Roberts, Y. Cao, A. D. Rollett, P. A. Salvador, *Acta Mater.* **2007**, *55*, 6159.
[65] L. Yang, V. Yadav, J. Melville, J. B. Harley, A. R. Krause, M. R. Tonks, *Mater. Des.* **2024**, *239*, 112763.
[66] D. Zöllner, *Comput. Mater. Sci.* **2021**, *187*, 110104.
[67] D. Zöllner, I. Zlotnikov, *Comput. Mater. Sci.* **2018**, *155*, 180.
[68] D. Zöllner, *Comput. Mater. Sci.* **2014**, *86*, 99.
[69] D. Zöllner, I. Zlotnikov, *Adv. Theory Simul.* **2019**, *2*, 1900064.
[70] S. A. Wright, S. J. Plimpton, T. P. Swiler, in *Potts-Model Grain Growth Simulations: Parallel Algorithms and Applications*, Sandia National Lab. (SNL-NM), Albuquerque, NM, USA, **1997**.
[71] D. Raabe, *Acta Mater.* **2000**, *48*, 1617.